Current-phase relation of a short multi-mode Bi<inf>2</inf>Se<inf>3</inf> topological insulator nanoribbon Josephson junction with ballistic transport

N.B. When citing this work, cite the original published paper.

(article starts on next page)

PAPER • OPEN ACCESS

Current-phase relation of a short multi-mode Bi$_2$Se$_3$ topological insulator nanoribbon Josephson junction with ballistic transport modes

To cite this article: Ananthu P Surendran *et al* 2023 *Supercond. Sci. Technol.* **36** 064003

View the article online for updates and enhancements.

Current-phase relation of a short multi-mode Bi₂Se₃ topological insulator nanoribbon Josephson junction with ballistic transport modes

Ananthu P Surendran[1] ⓘ**, Domenico Montemurro**[1,2] ⓘ**, Gunta Kunakova**[1,3] ⓘ**,**
Xavier Palermo[1] ⓘ**, Kiryl Niherysh**[1,3] ⓘ**, Edoardo Trabaldo**[1] ⓘ**, Dmitry S Golubev**[4] ⓘ**,**
Jana Andzane[3] ⓘ**, Donats Erts**[3] ⓘ**, Floriana Lombardi**[1] ⓘ **and Thilo Bauch**[1,*] ⓘ

[1] Quantum Device Physics Laboratory, Department of Microtechnology and Nanoscience, Chalmers University of Technology, SE-41296 Gothenburg, Sweden
[2] Dipartimento di Fisica 'Ettore Pancini,' Università degli Studi di Napoli Federico II, I-80125 Napoli, Italy
[3] Institute of Chemical Physics, University of Latvia, Raina Blvd. 19, LV-1586 Riga, Latvia
[4] QTF Centre of Excellence, Department of Applied Physics, Aalto University, PO Box 15100, FI-00076 Aalto, Finland

E-mail: bauch@chalmers.se

CrossMark

Abstract
We used the asymmetric superconducting quantum interference device (SQUID) technique to extract the current phase relation (CPR) of a Josephson junction with a 3D-topological insulator (3D-TI) Bi₂Se₃ nanobelt as the barrier. The obtained CPR shows deviations from the standard sinusoidal CPR with a pronounced forward skewness. At temperatures below $200\,\mathrm{mK}$, the junction skewness values are above the zero temperature limit for short diffusive junctions. Fitting of the extracted CPR shows that most of the supercurrent is carried by ballistic topological surface states (TSSs), with a small contribution of diffusive channels primarily due to the bulk. These findings are instrumental in engineering devices that can fully exploit the properties of the topologically protected surface states of 3D TIs.

Keywords: topological insulator, Josephson junction, SQUID, current phase relation

(Some figures may appear in colour only in the online journal)

---

* Author to whom any correspondence should be addressed.

1. Introduction

Topological superconductivity and Majorana zero-energy modes have attracted vast interest over the past few years owing to their potential for topologically-protected quantum information processing [1–3]. Hybrid devices involving a conventional s-wave superconductor (S) in proximity to a semiconducting nanowire with strong spin–orbit coupling [4, 5] or an unconventional metal such as a 3D topological insulator (3D-TI) [6–8] are expected to provide platforms for emulating and studying this exotic phenomena. One of the standard implementations of such hybrid devices includes S-3DTI-S junctions that exploit the topological surface states (TSSs) for hosting Majorana bound states (MBSs). Over the past decade, such Josephson junctions based on TI materials have been fabricated and extensively studied experimentally [9–30]. Here, Majorana physics manifests as peculiar properties of a part of the Andreev bound states (ABSs) carrying the Josephson current across the junction, namely MBSs. In an S-TI-S junction with multiple transport modes, MBSs are gapless even for not perfectly transparent S-TI interferences, and under proper conditions, they should show a 4π periodic current phase relation (CPR) coexisting with a 2π periodic CPR due to conventional ABS [7, 8, 31, 32]. The two periodicities should be reflected in the total CPR of the junction, and by probing it one could get access to the unconventional physics of MBSs [9–25, 27–30].

The CPR of the junction can be probed using various DC and RF measurement techniques. These include current biased asymmetric DC-superconducting quantum interference devices (SQUIDs) [12, 13, 22, 33–38], and magnetic field pattern measurements of single junctions [9, 36, 39–41], phase-controlled junctions [19], microwave-induced Shapiro steps [14–16, 18, 27, 30, 42–45] and RF-SQUIDs coupled to microwave resonator readouts [46, 47]. However, the critical point to note when looking for a 4π periodic CPR of MBSs is that if the temporal variation of the phase across the junction is slower compared to the inelastic scattering time or the quasi-particle poisoning time, these processes will restore the 2π periodicity of the CPR [7, 48]. As a result, the recent studies aimed at detecting MBSs based on TI-junctions primarily focus on Shapiro step measurements at frequencies larger than any relaxation or poisoning rate [14–16, 18, 27, 30] or microwave probing of phase-biased Josephson junctions [46]. The missing of odd integer Shapiro steps were reported, pointing toward the possible presence of 4π periodic modes in TI junctions [14–16, 18, 27, 30, 42, 43, 45].

A significant obstacle in revealing MBSs using Josephson junctions based on 3D-TI like Bi_2Se_3, Bi_2Te_3, and Sb_2Te_3 is the coexistence of bulk states in addition to the TSSs, making the electrical transport analysis cumbersome [6, 49]. Compensation doping has been used to reduce the bulk contribution, however, at the expense of electron mobility [10, 20–22, 24, 25, 27–29]. Another approach for reducing the bulk contribution to the electric transport is to increase the surface-to-volume ratio of the 3D TI by growing the material in the shape of nanowires or nanobelts [50–52]. Previous studies have shown high-quality interfaces between 3D-TI Bi_2Se_3

nanobelts and Al electrodes. These Josephson junctions show multiple Andreev reflections and large excess currents in the IVCs [17, 23]. Here, we further explore the properties of these junctions. Since the results we present here are based on DC measurements, we do not expect to observe any signature of MBS in the Josephson properties [7, 48]. Rather, our study is aimed at characterizing ABS in 3D-TI nanobelt-based junctions.

In this work, we study the CPR of a Bi_2Se_3 nanobelt-based Josephson junction embedded in an asymmetric dc-SQUID. To keep the analysis simple, we focus on junctions in the short limit where the superconducting coherence length ξ is larger than the length of the junction l. Here the ABSs dispersion takes a simple form given by $E_n = \pm\Delta[1 - \tau_n \sin^2(\varphi/2)]^{1/2}$, where Δ is the superconducting gap, E_n and τ_n correspond to the Andreev level energy and transmission probability of the nth mode, respectively, and φ is the phase difference across the junction [53]. The corresponding CPR of a short junction can be written as,

$$I(\varphi) = \frac{e\Delta(T)}{2\hbar} \sum_{n=1}^{N} \frac{\tau_n \sin(\varphi)}{[1 - \tau_n \sin^2(\varphi/2)]^{1/2}}$$

$$\times \tanh\left(\frac{\Delta(T)}{2k_B T}[1 - \tau_n \sin^2(\varphi/2)]^{1/2}\right) \quad (1)$$

where T is the temperature, $\Delta(T)$ is the corresponding superconducting gap, $\hbar$, k_B, and e are the reduced Planck constant, Boltzmann constant, and electron charge, respectively. In the above equation, the sum is taken over all transport modes in the TI junction. In TI nanobelts, spatial confinement along the transversal direction results in the formation of electronic subbands and a gap at the Dirac node [23, 27]. This prevents the observation of a perfectly transmissive transport mode. Even though we should not expect a mode with transparency 1, one should still be able to observe the contributions of transport modes with transparency close to one due to the peculiar linear Dirac dispersion in the surface states modes. The demonstration of these high transparency modes is the main objective of this paper.

2. Methods

The asymmetric dc-SQUID measurement is a powerful technique to extract the CPR of Josephson junctions [21, 22, 33, 54, 55]. Here, the test junction with unknown CPR $I_t = I_{t,c} \cdot f(\varphi_t)$ is integrated into a dc-SQUID layout along with a reference junction with known CPR $I_r = I_{r,c} \cdot g(\varphi_r)$ and sufficiently higher critical current $I_{r,c}$, typically 15–20 times larger than the critical current of the test junction $I_{t,c}$, see figure 1(a). Here φ_t and φ_r are the phases across the test and reference junctions, respectively. If the inductance of the SQUID loop, L, is small enough such that the screening parameter $\beta_L = (I_{r,c} + I_{t,c})L/\Phi_0 \ll 1$, upon application of an external magnetic flux, Φ_{ext}, the phase across the test junction is given by $\varphi_t \simeq \varphi_r + 2\pi\Phi_{ext}/\Phi_0$, with Φ_0 the superconductive
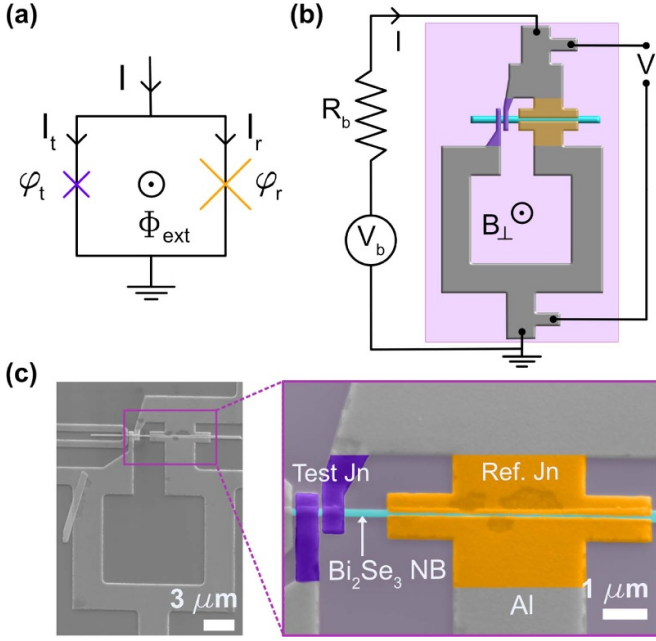
Figure 1. (a) Sketch of the SQUID containing both the test (purple) and reference (orange) junction (b) Layout of the SQUID with both the test and reference junction made from the same Bi_2Se_3 nanobelt. The current–voltage characteristic is measured using a four-point setup. (c) Scanning electron microscopy (SEM) image of the SQUID device (left panel). The right panel is a false-colored SEM image showing the test (purple) and reference (orange) junctions formed out of a Bi_2Se_3 nanobelt (cyan).

flux quantum [33]. Due to the large asymmetry of the critical currents, the phase across the reference junction remains approximately constant in applied magnetic flux. Therefore the maximum critical current of the SQUID is obtained for $I_r = I_{r,c}$ at $\varphi_{r,max}$, where the current through the reference junction is maximized, while the phase across the test junction, φ_t, varies approximately linearly with Φ_{ext} [33]. Thus, the CPR of the test junction can be determined by subtracting the constant contribution of the reference junction, $I_{r,c}$, assuming a point-like junction, from the total critical current of the SQUID and going from flux to phase following the relation,

$$\varphi_t \simeq \varphi_{r,max} + \frac{2\pi\Phi_{ext}}{\Phi_0}. \tag{2}$$

For a tunnel-like reference junction, one gets $\varphi_{r,max} = \pi/2$. However, for our devices, the reference junction is not a conventional tunnel junction. Indeed, nano-processing steps, especially the ones involving heating or etching, tend to alter the properties of TI materials. Therefore we opted to use only a single lithography step to reduce damage to the TI- junctions during device fabrication. In this case, even though the CPR of the reference junction is not known *a priori*, as long as $I_{r,c} \gg I_{t,c}$, one can still extract the CPR of the test junction. However, in this case $\varphi_{r,max}$ is not $\pi/2$. Earlier experiments have shown that this approach is reliable for extracting the CPR of the test junction [38, 54, 55].

We have realized Josephson junctions using Bi_2Se_3 nanobelts, grown by physical vapor deposition, which are at least 7–8 μm long to be able to fabricate both the test and reference junction on the same nanobelt [17, 26]. The fabrication process involves the dry transfer of nanobelts to a SiO_2/Si substrate followed by electron beam lithography and metallization. Following our previous works, before e-beam evaporation of the Pt(3 nm)/Al(80–100 nm) electrodes, a mild Ar ion milling is performed to remove the native oxide on the nanobelts [11, 17, 23]. SEM images of the SQUID device are shown in figure 1(c). Here, the length and width of the reference junction are defined by the separation between the two Al electrodes and the dimension of the electrodes along the longitudinal direction of the nanobelt, respectively. In contrast, the width of the test junctions is fixed by the width of the nanobelt (see figure 1).

3. Results and discussion

We will focus on measurements from a single representative SQUID (BSH13 A3S2) formed from a Bi_2Se_3 nanobelt of width $w \simeq 188$ nm (from SEM in-lens image) and thickness $t \simeq 48$ nm (from AFM image, data not shown). Similar behavior has been observed in other devices (data not shown). The test junction has a length $l \simeq 83$ nm, and the corresponding width and length of the reference junction are $\simeq 5\,\mu$m and $\simeq 80$ nm, respectively. For the ballistic case ($l <$ mean free path $\simeq 200$ nm [50]), the coherence length can be estimated using $\xi = \hbar v_F/\Delta'$, with $v_F \simeq 5 \times 10^5\,m\,s^{-1}$ the Fermi velocity of the surface states in Bi_2Se_3, [50, 51] and Δ' the induced superconducting gap in the surface state. For a typical $\Delta' \simeq 135\,\mu$eV extracted from single junction devices [17] we obtain $\xi \simeq 2.4\,\mu$m, which is much longer than the length of our junctions, placing them in the short junction limit [53]. The SQUID loop line width is kept at 3 μm in most sections of the loop to minimize kinetic inductance contributions, and thus have $\beta_L < 1$. From the layout of the SQUID loop, by numerically solving the London-Maxwell equations we determined the effective area $A_{eff} \simeq 200\,\mu$m^2. This results in a modulation period of approximately 10 μT. From the same numerical calculations, we also extract a SQUID loop inductance value $L \simeq 29$ pH, of which ~27 pH correspond to the geometric inductance, and the remaining ~2 pH are the kinetic contribution to loop inductance [56]. Here we used a London penetration depth of $\lambda = 70$ nm, typical for 100 nm thick Al films [57]. Unless mentioned, all the measurements were carried out in a dilution refrigerator with a base temperature of 19 mK. The measurement lines are equipped with RC filters at the 4 K stage and copper powder filters at the mixing chamber stage to minimize environmental noise/radiation reaching the device.

We measured the current–voltage characteristic (IVC) of the SQUID for various externally applied magnetic fields. The IVC of the TI SQUID at zero applied magnetic field is given in figure 2(a). Here, one can see the typical hysteretic IVC of Al-Bi_2Se_3-Al junctions, and we attribute the origin of this
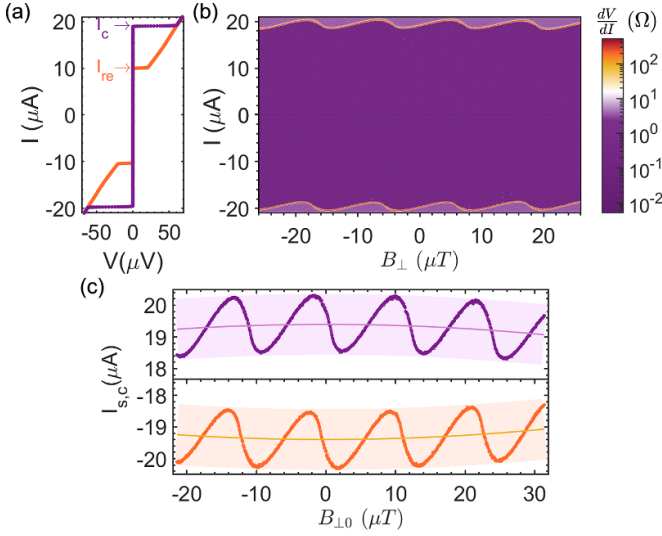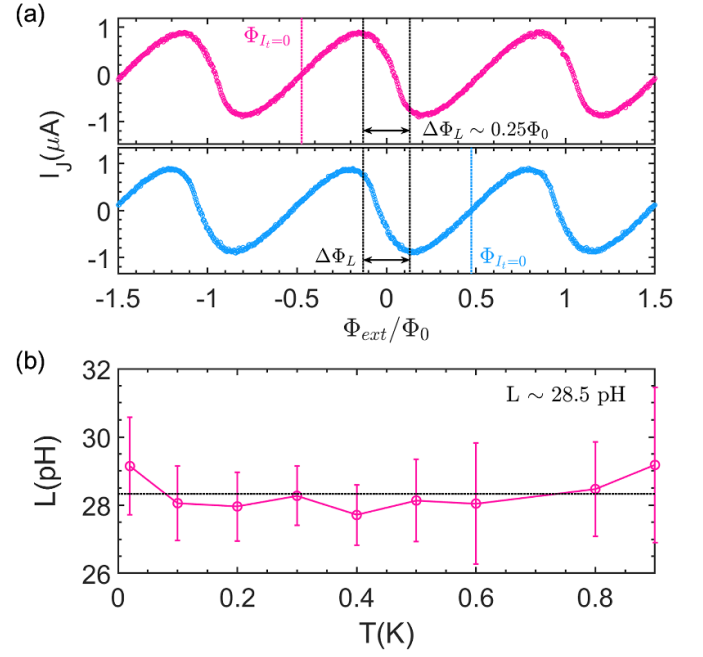
Figure 2. (a) Current–voltage characteristics at $T = 20$ mK with zero applied magnetic field. The arrows indicate the direction of the sweep (starting from zero), and the IVC shows hysteretic behavior . Here, I_c and I_{re} correspond to the critical current and retrapping current of the device, respectively. (b) Differential resistance of the SQUID as a function of bias current and externally applied magnetic field measured at $T = 20$ mK. (c) The critical current of the SQUID for positive (upper panel) and negative (lower panel) bias current. The light-colored lines indicate the background envelope from the magnetic field pattern of the reference junction. Here we adjusted the magnetic field data for a constant offset, B_{off}, to $B_{0\perp} = B_\perp + B_{off}$, with $B_\perp$ the applied magnetic field (see panel (a)) and $B_{off} \simeq 5\,\mu$T. Here, the offset was determined from the measured magnetic field position of the maxima of the background envelope (Fraunhofer pattern).

Figure 3. (a) Extracted current-flux relation of the TI test junction at $T = 20$ mK for both positive (magenta) and negative (blue) current bias directions of the asymmetric TI-SQUID and corresponding arrows indicate the location of maxima of CΦR. The shift in the location of positive and negative maxima from integer Φ_{ext}/Φ_0 positions due to finite inductance can be quantified in terms of $\Delta\Phi_L = L(I_{r,c} - I_{t,c})$, with $(I_{r,c} - I_{t,c})/2$ being the circulating current in the SQUID loop. (b) Loop inductance of the SQUID estimated using $\Delta\Phi_L$ as a function of bath temperature. The error bars represent the standard deviations of L obtained from different pairs of the CΦR maxima corresponding to various integer Φ_{ext}/Φ_0 locations that are used for estimating $\Delta\Phi_L$. As one can see, L remains constant around the value of 29 pH confirming that it is dominated by the geometric inductance of the device.

hysteresis to heating effects [17, 58]. Now, to get the critical current(I_c) of the device, we need to consider the bias sections of the IVC when the junction switches from the superconducting state to the resistive state (in both positive and negative bias directions), which are plotted in purple in figure 2(a). For the rest of the analysis, we will ignore the sections of IVC where the junction goes back from the resistive state to the superconducting state (plotted in orange in figure 2(a)), as the switch occurs at the retrapping current (I_{re}), which is lower than the critical current of the device. Figure 2(b) shows the variation of the differential resistance dV/dI of the TI-SQUID with respect to the applied bias current I and external magnetic field $B_\perp$. Here, one can clearly see the modulations of the critical current from the asymmetric SQUID (bright lines).

Next, we determined the critical current of the SQUID, $I_{s,c}$, from the IVC for every applied magnetic field by setting a threshold voltage of $3\,\mu$V as the criteria for detecting the switch from the superconducting state to the normal state. The resulting modulation of the positive and negative critical currents are shown as closed symbols in figure 2(c). On top of the SQUID modulations, we observe a background envelope (solid lines) arising from the magnetic field modulation of the critical current $I_{r,c}$ of the reference junction (Fraunhofer pattern). Upon close examination, one could see that the maxima of the Fraunhofer patterns on both positive and negative sides occurred at the field of $-5\,\mu$T. This means we have a

constant offset in the magnetic field at the device. We see the same magnetic field offset in every measurement that we perform using the setup. To account for this shift, the magnetic field scale in figure 2(c) is offset to $B_{0\perp} = B_\perp + B_{off}$. From the maxima of the Fraunhofer pattern, we get $I_{r,c}$ to be 19.4 μA. Now, by removing the background due to the reference junction from the total response of the SQUID, one obtains the current modulations of the test junction (I_J) as a function of $B_{0\perp}$. By converting from magnetic field to flux, $\Phi_{ext} = B_{0\perp}A_{eff}$ using the observed modulation period of $\simeq 11.6\,\mu$T corresponding to one flux quantum Φ_0, we obtain the current–flux relation (CΦR) of our test junction for the positive and negative bias currents, as shown in figure 3(a). From here, we get $I_{t,c} \approx 880$ nA, and the critical current asymmetry in our SQUID device is $I_{r,c}/I_{t,c} \approx 22$, which is large enough for a proper CPR extraction. Using the simulated value of loop inductance, we can estimate the screening parameter $\beta_L \simeq 0.28$, which is not $\ll 1$, and we will have to account for finite inductance effects when extracting the CPR.

In the following, we will look at the effect of inductance on the extracted CΦRs and thereby estimate the inductance of the SQUID loop experimentally. From equation (2), one can see that for the negligible inductance case, when the
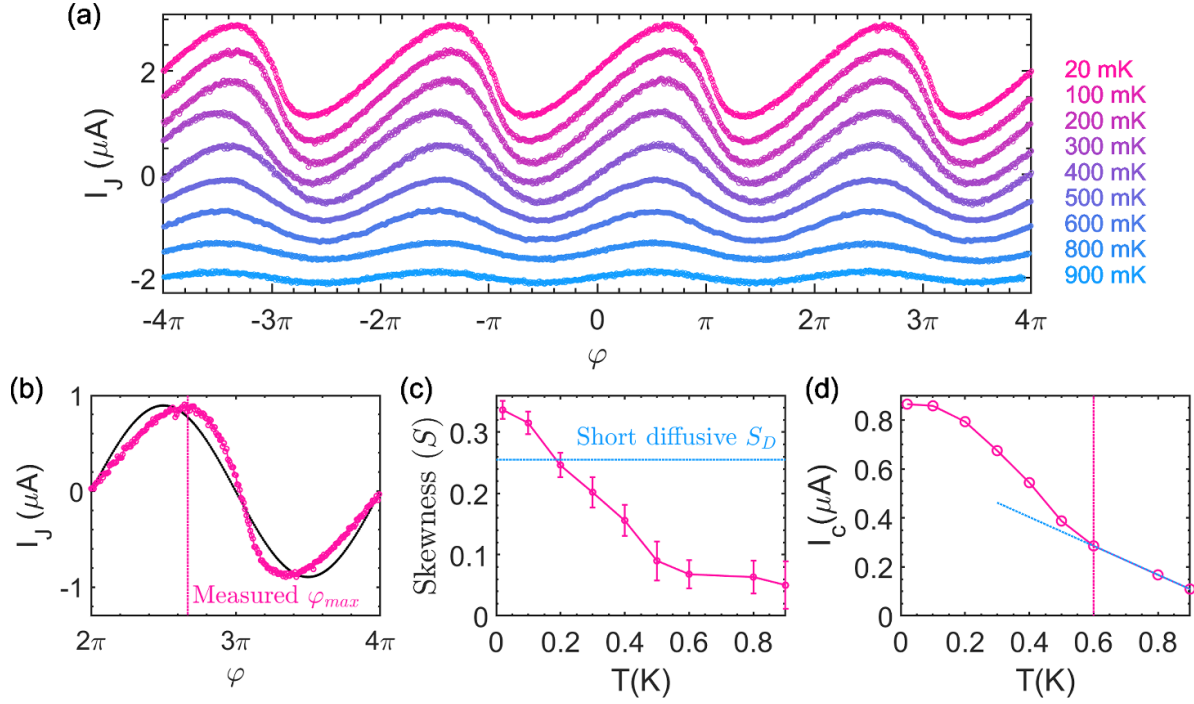
Figure 4. (a) Evolution of the extracted CPR of the TI test junction with varying temperature. (b) Extracted CPR at 20 mK (magenta) along with a sinusoidal curve with the same amplitude (black) to emphasize the deviation of CPR from the conventional case. The vertical dotted magenta line indicates the location of φ_{max} for the measured CPR. (c) Plot showing measured skewness of CPR vs. temperature. Below 200 mK the S is greater than the zero temperature limit S_D, and the transport of the junction cannot be explained fully by pure diffusive transport modes. (d) The critical current of the test junction as a function of temperature is shown. The open symbols are the measured data extracted from the CPRs shown in panel (a). The dotted line is the change in the slope of I_c vs T curve, indicating the presence of two different types of transport modes with a higher (around T_c of Al, 1.15 K) and a lower (around 600 mK) critical temperature.

external flux is an integer multiple of Φ_0, we get $\varphi_t \simeq \varphi_{r,max}$. Now, if we assume the CPRs of the test and reference junction have the same functional shape, $f(\varphi) \simeq g(\varphi)$, the CΦRs will have the maxima at external flux values which are an integer multiple of Φ_0. But as seen from figure 3(a), the maxima (in both positive and negative current directions as indicated by the magenta and blue arrows respectively) are offset from integer Φ_{ext}/Φ_0 values. This shift in the CΦRs is due to the field produced by the circulating current in the SQUID loop, and can be accounted for by modifying the equation for the phase across the test junction as $\varphi_t = \varphi_r + 2\pi\Phi/\Phi_0$ with $\Phi = \Phi_{ext} - L[I_r(\varphi_r) - I_t(\varphi_t)]/2$ the total magnetic flux through the SQUID loop [37], assuming the inductance is distributed equally ($L/2$) among the two arms of the SQUID. This shift depends on the direction of the bias current through the SQUID loop, and in our case, the CΦRs are shifted to the left (right) for positive (negative) bias current. Now to quantify this, for every integer Φ_{ext}/Φ_0 positions, one can define a parameter $\Delta\Phi_L$ as the distance between the observed location of the maxima pair corresponding to positive and negative current bias (see the black dotted lines in figure 3(a)). From the equation for φ_t in the finite inductance case, it is straightforward to see that $\Delta\Phi_L = L(I_{r,c} - I_{t,c})$, with $(I_{r,c} - I_{t,c})/2$ the circulating current in the loop when the SQUID critical current is maximized [37]. In our device, by considering four pairs of peaks in the CΦR (only three are shown for clarity), we obtain $\Delta\Phi_L \simeq 0.28\,\Phi_0$ corresponding to a loop inductance

value of roughly 29 pH. This value is in good agreement with the L value that we find from our numerical simulations [56]. In figure 3(b) we show the extracted SQUID loop inductance for various temperatures up to 900 mK. Here, within the error bars of our data, we do not see a considerable increase in the inductance of the SQUID loop with temperature, confirming that the geometric inductance dominates the loop inductance in the entire temperature range.

To convert the magnetic flux to the phase drop across the test junction, one should, in principle use equation (2). However, as discussed above, this equation is only valid for zero loop inductance. To account for the finite inductance, we need to subtract from equation (2) the flux shift due to the circulating current. This can be obtained by subtracting the magnetic flux value at which the current of the test junction goes to zero $\varphi_t = 2\pi(\Phi_{ext} - \Phi_{I=0})/\Phi_0$ flux (see magenta and blue dotted lines in figure 3(a)), which accounts for both $\varphi_{r,max}$ and the contribution of the circulating current. The resulting CPRs at various temperatures are shown in figure 4(a). Note that these are not the true CPRs of the test junction. This is because for finite β_L, the flux to phase conversion is not completely linear as in equation (2), and deviations from the linear trend occur around odd multiple integers of π (see discussion below) [37]. Also, from here on, we use φ instead of φ_t to indicate the phase across the test junction extracted assuming linear flux to phase conversion and reserve φ_t to indicate the actual phase across the test junction.

As seen in figure 4(a), at low temperatures, the extracted CPRs are forward skewed and evolve into a more sinusoidal CPR at higher temperatures. One commonly used method to quantify the departure of CPRs from a conventional sinusoidal CPR is by defining the skewness, $S = (2\varphi_{\max}/\pi) - 1$, where $\varphi_{\max}$ corresponds to the phase at which the critical current of the junction is reached [22, 47, 54]. The maximum skewness $S = 1$ with $\varphi_{\max} = \pi$ is achieved for transmission probability $\tau_n = 1$ (see equation (1)), whereas for $\tau_n \ll 1$ one obtains $S = 0$ (sinusoidal CPR). We find that at 20 mK, $\varphi_{\max} = 0.67\pi$, which corresponds to a skewness $S = 0.34$ (see figure 4(b)). Here, we can rule out any inductance contributions to the position of $\varphi_{\max}$, since in the limit of a small screening parameter the CPR is affected only in a small phase region around odd integer multiples of π (see below). In figure 4(c) we show the monotonic decrease of the skewness S with increasing temperature, asymptotically approaching zero for higher temperatures. We can now compare the skewness parameter to the predictions for different junction regimes. For a short diffusive junction, $\xi < l$, with $\xi = \sqrt{\hbar D/\Delta'}$ the coherence length, D the diffusion constant, and Δ' the induced superconducting gap, one expects skewness $S_D = 0.255$ (see dotted line in figure 4(c)) [47]. We clearly observe that for temperatures below 200 mK, the transport in our TI junction cannot be described by pure diffusive transport. In the limit of Josephson transport coming only from the surface TI channels (TI surface modes) one can estimate the skewness by calculating the CPR using equation (1) and the transmission probabilities τ following [59], assuming an extreme chemical potential mismatch between the TI channel and the TI covered by the Al electrode,

$$\tau_n = \frac{k_n^2}{k_n^2 \cos^2(k_n l) + k_F^2 \sin^2(k_n l)} \quad (3)$$

with quantized electron momentum $k_n = \sqrt{k_F^2 - k_y^2}$ along longitudinal direction, where k_F is the Fermi wave vector and k_y the quantized transverse momentum given by $k_y = 2\pi(n + \frac{1}{2})/C$ with $n = 1, 2, 3\ldots$ and C being the circumference of the nanobelt ($2(w + t)$). Here we obtain $S = 0.41$ at 20 mK. The fact that the observed skewness parameter is smaller than the one expected for the Josephson current carried exclusively by the surface state suggests that bulk states contribute to the overall current as well. This is supported by the temperature dependence of the critical current (I_c) of the test junction shown in figure 4(d). The open symbols are the measured data extracted from the CPRs shown in figure 4(a). As indicated by the dashed lines, around 600 mK we observe a drastic change in the slope of the I_c vs T curve that might be due to the presence of two different types of Josephson transport channels with different T_C values as reported in [20, 27]. The Josephson current contribution with higher T_C (same as the Al electrode, $T_C = 1.15$ K) can be attributed to the ballistic TSSs, while the Josephson current contribution that vanishes fast around 600 mK could be attributed to the diffusive transport modes due to bulk states. This is further supported by the low bulk mobility values we extract from magnetotransport data [51].

To estimate the individual contributions from the bulk states and surface states to the total Josephson current, we fit the CPR measured at 20 mK (see closed symbols in figure 5(c)) with a two-band model. For the Josephson current carried by the TSSs we again consider quantized transport modes with transmission probabilities dictated by the geometry of the device, following [59] (see equation (3)). After removing an oxide thickness of 5 nm from the width and thickness, we find for the nanoribbon used in the SQUID, $C = 452$ nm. Following our previous work, we only consider the modes that travel on the top surface of the TI-belt to be ballistic, as the modes that go around the circumference of the nanobelt suffer from poor mobilities due to the interface with the substrate [23, 51, 52] and/or the paths are longer than the phase coherence length. For the junction geometry, assuming a k_F of 0.55 nm^{-1} based on magnetotransport measurements performed by us on similar Bi$_2$Se$_3$ nanobelts [50–52], we find that in total there are 39 modes arising from TSSs. Out of these, 29 of them travel on the top surface and should be contributing to the ballistic portion of the supercurrent. In figure 5(b) we show the polar plot of the transmission probabilities as a function of (continuous) angle θ (see solid line) using equation (3), displaying Fabry–Pérot-like resonance features in the form of lobes with transmission probabilities very close 1 at certain θ values related to the geometry of the device [16, 27]. The transmission probabilities of the individual quantized transport modes are shown as open symbols. The orange open symbols correspond to the τ values of modes that are on the top surface of the junction (up to $\theta \approx 48°$). More than half of these modes have τ values close to 1, resulting in an average value of 0.92 for the modes on the top surface. The modes with θ above 48° (purple open symbols) that go around the circumference are not ballistic as discussed in [23]. So we describe the Josephson current carried by modes that go around the nanobelt and those carried by the bulk states with a diffusive multi-mode model using the Dorokhov distribution of transmission probabilities [60] given by,

$$\rho(\tau) = \frac{\pi \hbar G_N}{2e^2} \frac{1}{\tau\sqrt{1 - \tau}} \quad (4)$$

where G_N is the normal-state conductance for diffusive modes. Since the value of G_N is unknown, we take it as a fitting parameter in our analysis. Now, the CPR contribution from the diffusive modes is calculated by replacing the sum in equation (1) with an integral in the interval $\tau = [0, 1]$ covering the full range of transmission probabilities.

The fitted contributions to the CPR of our junction at 20 mK are shown in figure 5(c). To fit the CPR, we had to assume a temperature ($T_{\mathrm{fit}} \simeq 195$ mK), which is higher than the bath temperature of 20 mK. This discrepancy may have its origins in elevated quasi-particle temperatures or additional current noise typically observed in SNS junctions [33, 61]. The details about noise contributions are beyond the scope of this work and will be described elsewhere. The best fit is obtained when out of the total critical current of ≈ 880 nA (see magenta circles corresponding to measured data or blue line corresponding to the sum of ballistic and diffusive parts) of the test
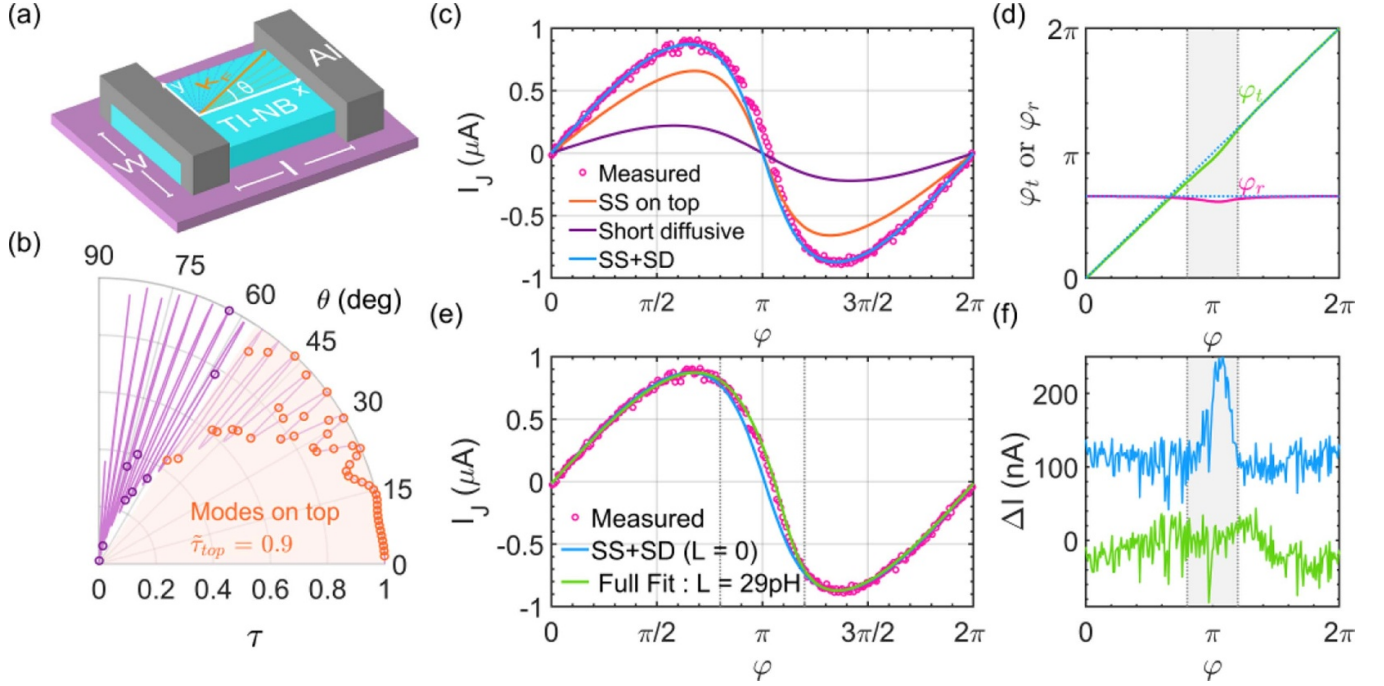
Figure 5. (a) Sketch of an S-TI-S junction showing quasi-particle trajectories in terms of the angle θ made with longitudinal momentum axis with $\theta = \tan^{-1}\left(\frac{k_x}{k_y}\right)$. (b) Angle-dependent transmission probabilities (Fabry–Pérot like resonance (*s*) of various transport modes in our junction, assuming extreme chemical potential mismatch at the interface). The orange circles correspond to the modes which are fully contained on the top surface of the junction, and the purple dots correspond to the modes that propagate around the nanobelt's perimeter. (c) Measured CPR of the junction at 20 mK (magenta circles) along with fitted curves assuming zero inductance, $L = 0$. The orange curve is the current contribution from the ballistic TSSs on the top surface of the junction, and the purple line shows the diffusive contributions to the CPR. The sum of both ballistic and diffusive modes is given as the blue curve. (d) Variation of φ_t and φ_r with respect to φ, the extracted phase across the junction assuming a linear variation of phase with Φ_{ext}. Most of the deviation occurs around $\varphi \simeq \pi$ (see the shaded region, $0.8\pi - 1.2\pi$). (e) Measured CPR of the junction (magenta circles) along with the fitted curve considering a finite loop inductance of $L = 29$ pH (green line). The zero inductance fit is given for comparison (blue). The region in between the dashed gray lines corresponds to regions mostly affected by inductance as in panel (d), whereas φ_{max} of the CPR lies outside this region. (f) Difference or residual between the measured data and fit ($\Delta I = I_J - I_{fit}$). The data are offset for clarity. For the zero inductance case, there is a peak in ΔI around π, indicating the deviation of the fitted curve around π from the measurement data. The green curve corresponds to the fit including the loop inductance resulting in a pronounced reduction of the peak around π. The shaded region is the same as in panel (d).

junctions, ≈ 657 nA are carried by ballistic TSSs on the top of the junction (orange line), and ≈ 223 nA are carried by the diffusive transport modes (purple line). The presence of diffusive transport modes with lower skewness will reduce the skewness of the overall CPR of the junction as compared to transport carried entirely by the TSS, in agreement with our experiment.

Finally, we discuss the influence of the finite inductance on the extracted CPR. As one can clearly see in figure 5(c), the measured CPR does not cross zero at $\varphi_t = \pi$. This is due to the breakdown of the linear mapping between external flux and phase across the test junction around phase values of odd integer multiples of π. To resolve this and obtain better flux to phase conversion, one must solve the equation $\varphi_t = \varphi_r + 2\pi\Phi/\Phi_0$ for each value of Φ_{ext}, including the finite SQUID loop inductance, to get the pairs of phase values φ_r and φ_t, that maximize the current through the SQUID loop [37]. The variation of φ_r and φ_t, calculated for a finite inductance value of $L = 29$ pH, with respect to φ is given in figure 5(d). Here one can see that the curves show deviations around π (shaded region) from the expected linear behavior (dashed blue lines) corresponding to zero inductance case. A similar

deviation visible in the difference between the measured CPR and the fitted curve is given in figure 5(f) in the form of a peak around π. Now using φ_t values, that include inductance effects, we can reproduce the measured CPR relation more accurately and reproduce the zero crossing of the CPR at a phase value slightly larger than π as seen in figure 5(e). This is also reflected in the residual from the fit including the finite inductance of the SQUID loop (see figure 5(f)). In fact, the peak around π disappears, leaving behind mostly the noise from the measurement. Finally, the true CPR of our TI-junction is represented by the blue curve corresponding to the zero inductance fit in figures 5(c) and (e), and the deviation of the measured CPR from the theoretically expected CPR is simply caused by not fully satisfying the condition $\beta_L \ll 1$. Here, we note that the finite inductance value does not significantly affect the phase position of the maximum of the CPR (see figure 5(e)), since the position of the maximum and minimum of the CPR are outside the phase region (in between the dashed gray lines in figures 5(d)–(f) where φ_t deviates from the linear dependence on φ). Therefore, the various skewness values we extracted earlier are still valid, indicative of the short quasi-ballistic nature of our junction.

4. Conclusions

To conclude, we extracted the CPR of Al-Bi$_2$Se$_3$-Al junctions formed out of 3D-TI nanobelts using asymmetric SQUID measurements. We observe a skewed CPR due to the TSSs hosting transport modes with high transmission probabilities. We found that our junctions are, in the short, quasi-ballistic regime, with most supercurrent being carried by ballistic TSSs. However, to fit the extracted CPR, one has to consider both ballistic and diffusive contributions. Therefore, reducing the number of transport modes in these junctions is essential, especially the diffusive bulk contributions, in order to ensure fewer ambiguities in future experiments aimed at detecting MBSs using 3D-TI materials-based devices.

Data availability statement

All data that support the findings of this study are included within the article (and any supplementary files). Additional data are available from the corresponding author upon reasonable request.

Acknowledgments

ORCID iDs

Ananthu P Surendran https://orcid.org/0000-0002-0949-4145
Domenico Montemurro https://orcid.org/0000-0001-8944-0640
Gunta Kunakova https://orcid.org/0000-0003-0243-2678
Xavier Palermo https://orcid.org/0000-0001-9997-3053
Kiryl Niherysh https://orcid.org/0000-0002-9861-9957
Edoardo Trabaldo https://orcid.org/0000-0002-0188-6814
Dmitry S Golubev https://orcid.org/0000-0002-0609-8921
Jana Andzane https://orcid.org/0000-0002-9802-6895
Donats Erts https://orcid.org/0000-0003-0345-8845
Floriana Lombardi https://orcid.org/0000-0002-3478-3766
Thilo Bauch https://orcid.org/0000-0002-8918-4293

References

[1] Kitaev A Y 2002 *Ann. Phys., NY* **303** 2–30
[2] Nayak C, Simon S H, Stern A, Freedman M and Das Sarma S 2008 *Rev. Mod. Phys.* **80** 1083–159
[3] Sarma S D, Freedman M and Nayak C 2015 *npj Quantum Inf.* **1** 15001
[4] Lutchyn R M, Sau J D and Das Sarma S 2010 *Phys. Rev. Lett.* **105** 1–4
[5] Mourik V, Zuo K, Frolov S M, Plissard S R, Bakkers E P and Kouwenhoven L P 2012 *Science* **336** 1003–7
[6] Hasan M Z and Kane C L 2010 *Rev. Mod. Phys.* **82** 3045–67
[7] Fu L and Kane C L 2009 *Phys. Rev.* B **79** 1–4
[8] Tkachov G 2019 *Phys. Rev.* B **100** 1–8
[9] Williams J R, Bestwick A J, Gallagher P, Hong S S, Cui Y, Bleich A S, Analytis J G, Fisher I R and Goldhaber-Gordon D 2012 *Phys. Rev. Lett.* **109** 1–5
[10] Cho S, Dellabetta B, Yang A, Schneeloch J, Xu Z, Valla T, Gu G, Gilbert M J and Mason N 2013 *Nat. Commun.* **4** 1–6
[11] Galletti L *et al* 2014 *Phys. Rev.* B **89** 1–9
[12] Kurter C, Finck A D, Hor Y S and Van Harlingen D J 2015 *Nat. Commun.* **6** 2–7
[13] Sochnikov I *et al* 2015 *Phys. Rev. Lett.* **114** 1–6
[14] Wiedenmann J *et al* 2016 *Nat. Commun.* **7** 1–7
[15] Bocquillon E, Deacon R S, Wiedenmann J, Leubner P, Klapwijk T M, Brüne C, Ishibashi K, Buhmann H and Molenkamp L W 2017 *Nat. Nanotechnol.* **12** 137–43
[16] Li C, de Boer J C, de Ronde B, Ramankutty S V, van Heumen E, Huang Y, de Visser A, Golubov A A, Golden M S and Brinkman A 2018 *Nat. Mater.* **17** 875–80
[17] Kunakova G, Bauch T, Trabaldo E, Andzane J, Erts D and Lombardi F 2019 *Appl. Phys. Lett.* **115** 172601
[18] Le Calvez K, Veyrat L, Gay F, Plaindoux P, Winkelmann C B, Courtois H and Sacépé B 2019 *Commun. Phys.* **2** 1–9
[19] Ren H *et al* 2019 *Nature* **569** 93–98
[20] Schüffelgen P *et al* 2019 *Nat. Nanotechnol.* **14** 825–31
[21] Kayyalha M, Kargarian M, Kazakov A, Miotkowski I, Galitski V M, Yakovenko V M, Rokhinson L P and Chen Y P 2019 *Phys. Rev. Lett.* **122** 47003
[22] Kayyalha M, Kazakov A, Miotkowski I, Khlebnikov S, Rokhinson L P and Chen Y P 2020 *npj Quantum Mater.* **5** 1–7
[23] Kunakova G, Surendran A P, Montemurro D, Salvato M, Golubev D, Andzane J, Erts D, Bauch T and Lombardi F 2020 *J. Appl. Phys.* **128** 194304
[24] De Ronde B, Li C, Huang Y and Brinkman A 2020 *Nanomaterials* **10** 1–9
[25] Stolyarov V S *et al* 2020 *Commun. Mater.* **1** 1–11
[26] Kim N H, Kim H S, Hou Y, Yu D and Doh Y J 2020 *Curr. Appl. Phys.* **20** 680–5
[27] Rosenbach D *et al* 2021 *Sci. Adv.* **7** eabf1854
[28] Bai M, Wei X K, Feng J, Luysberg M, Bliesener A, Lippertz G, Uday A, Taskin A A, Mayer J and Ando Y 2022 *Commun. Mater.* **3** 1–7
[29] Schmitt T W *et al* 2022 *Nano Lett.* **22** 2595–602
[30] Fischer R, Picó-Cortés J, Himmler W, Platero G, Grifoni M, Kozlov D A, Mikhailov N N, Dvoretsky S A, Strunk C and Weiss D 2022 *Phys. Rev. Res.* **4** 1–9
[31] Cook A M, Vazifeh M M and Franz M 2012 *Phys. Rev.* B **86** 1–17
[32] Snelder M, Veldhorst M, Golubov A A and Brinkman A 2013 *Phys. Rev.* B **87** 1–7
[33] Della Rocca M L, Chauvin M, Huard B, Pothier H, Esteve D and Urbina C 2007 *Phys. Rev. Lett.* **99** 1–4
[34] Spanton E M, Deng M, Vaitiekėnas S, Krogstrup P, Nygård J, Marcus C M and Moler K A 2017 *Nat. Phys.* **13** 1177–81
[35] Murani A *et al* 2017 *Nat. Commun.* **8** 1–7
[36] Assouline A *et al* 2019 *Nat. Commun.* **10** 126
[37] Nichele F *et al* 2020 *Phys. Rev. Lett.* **124** 1–6
[38] Mayer W, Dartiailh M C, Yuan J, Wickramasinghe K S, Rossi E and Shabani J 2020 *Nat. Commun.* **11** 212
[39] Ghatak S, Breunig O, Yang F, Wang Z, Taskin A A and Ando Y 2018 *Nano Lett.* **18** 5124–31

[40] Chen A Q, Park M J, Gill S T, Xiao Y, Reig-i Plessis D, MacDougall G J, Gilbert M J and Mason N 2018 *Nat. Commun.* **9** 1–9

[41] Kononov A *et al* 2020 *Nano Lett.* **20** 4228–33

[42] Kwon H J, Sengupta K and Yakovenko V M 2004 *Eur. Phys. J. B* **37** 349–61

[43] Domínguez F, Kashuba O, Bocquillon E, Wiedenmann J, Deacon R S, Klapwijk T M, Platero G, Molenkamp L W, Trauzettel B and Hankiewicz E M 2017 *Phys. Rev. B* **95** 1–9

[44] Li C Z, Wang A Q, Li C, Zheng W Z, Brinkman A, Yu D P and Liao Z M 2020 *Phys. Rev. Lett.* **124** 156601

[45] Park J, Choi Y B, Lee G H and Lee H J 2021 *Phys. Rev. B* **103** 1–9

[46] Murani A, Dassonneville B, Kasumov A, Basset J, Ferrier M, Deblock R, Guéron S and Bouchiat H 2019 *Phys. Rev. Lett.* **122** 1–6

[47] Haller R *et al* 2022 *Phys. Rev. Res.* **4** 013198

[48] Badiane D M, Houzet M and Meyer J S 2011 *Phys. Rev. Lett.* **107** 1–5

[49] Kong D *et al* 2011 *ACS Nano* **5** 4698–703

[50] Andzane J, Kunakova G, Charpentier S, Hrkac V, Kienle L, Baitimirova M, Bauch T, Lombardi F and Erts D 2015 *Nanoscale* **7** 15935–44

[51] Kunakova G, Galletti L, Charpentier S, Andzane J, Erts D, Léonard F, Spataru C D, Bauch T and Lombardi F 2018 *Nanoscale* **10** 19595–602

[52] Kunakova G, Bauch T, Palermo X, Salvato M, Andzane J, Erts D and Lombardi F 2021 *Phys. Rev. Appl.* **16** 1

[53] Beenakker C W J 1991 *Phys. Rev. Lett.* **67** 3836–9

[54] Nanda G, Aguilera-Servin J L, Rakyta P, Kormányos A, Kleiner R, Koelle D, Watanabe K, Taniguchi T, Vandersypen L M and Goswami S 2017 *Nano Lett.* **17** 3396–401

[55] Thompson M D, Ben Shalom M, Geim A K, Matthews A J, White J, Melhem Z, Pashkin Y A, Haley R P and Prance J R 2017 *Appl. Phys. Lett.* **110** 162602

[56] Johansson J, Cedergren K, Bauch T and Lombardi F 2009 *Phys. Rev. B* **79** 1–6

[57] Romijn J, Klapwijk T M and Mooij J E 1981 *Physica* B+C **108** 981–2

[58] Courtois H, Meschke M, Peltonen J T and Pekola J P 2008 *Phys. Rev. Lett.* **101** 1–4

[59] Titov M and Beenakker C W 2006 *Phys. Rev. B* **74** 1–4

[60] Kos F, Nigg S E and Glazman L I 2013 *Phys. Rev. B* **87** 1–10

[61] Akazaki T, Nakano H, Nitta J and Takayanagi H 2005 *Appl. Phys. Lett.* **86** 1–3